# Model-based spectral reconstruction of interferometric acquisitions

Mohamad Jouni, Daniele Picone, Mauro Dalla Mura

# MODEL-BASED SPECTRAL RECONSTRUCTION OF INTERFEROMETRIC ACQUISITIONS

*Mohamad Jouni, Daniele Picone, Mauro Dalla Mura*

Univ. Grenoble Alpes, CNRS, Inria
Grenoble INP, GIPSA-lab
38000 Grenoble, France

## ABSTRACT

Spectral information of the scene can be reconstructed from processing observations acquired by interferometric devices. In the case of devices that have multiple wave interference (e.g., Fabry-Pérot etalons), a simple inversion such as inverse Fourier transform (e.g., for Michelson-like interferometers) of the measured interferograms is not straightforward due to the ill-posedness of the problem. In this paper, we represent the system through an $\infty$-wave model. The spectral reconstruction is done by a model-based approach as we have a good knowledge of the system. Specifically, we propose to use Loris-Verhoeven algorithm with proximal solvers and induced sparsity on the Fourier domain of the desired spectrum. Our proposal is more robust to noise compared to conventional reconstruction algorithms, as demonstrated by experiments that are carried with interferograms computed from real spectral acquisitions.

***Index Terms*—** Interferometry, inverse problems, interpretability, spectral reconstruction, model-based

## 1. INTRODUCTION

Characterizing the *spectrum* of a light source (i.e., measuring its intensity at each wavelength) is at the core of imaging spectroscopy, and has deep implications in various fields, such as geology, gas detection, security, remote sensing, disaster prevention, and more [1,2]. In recent times, both the scientific community and industrial venues have shown interest in image spectrometers which operate on the principle of *interferometry*, as they potentially allow for instruments with reduced cost and dimensions and for acquisitions with finer spectral resolution and improved SNR [3, 4].

In general, interferometry is a technique to measure the interference of superimposed coherent light waves which travel across different optical paths, known in the field as optical path differences (OPDs). The representation of the spectrum of incident waves in the domain of OPD is known as *interferogram*. Fourier-transform spectroscopy (FTS) defines a class of optical devices based on interferometry, which allow light waves to travel across different OPDs in order to capture a sampled version of this interferogram. Despite the potential benefits, the desired acquisitions are not immediately intelligible to the final user, as they are only available in a transformed domain. Therefore the problem must be approached as computational imaging system [5], as a data processing step is required in order to reconstruct the spectrum of the incident light source from the observed interferogram.

This work is partly supported by grant ANR FuMultiSPOC (ANR-20-ASTR-0006), and partly by Région Auvergne-Rhône-Alpes grant "Pack Ambition International 2021" (21-007356-01FONC, 21-007356-02INV).

The (ideally continuous) interferogram can be interpreted as a Fourier transformation of the original spectrum, and the reconstruction is customarily performed as an inverse transformation. However, two main issues arise: firstly, this model is just an approximation of the optical transformations that are performed by the instrument itself, and a more accurate description of such phenomena may be beneficial to the spectrum reconstruction. Secondarily, applying such methods blindly does not take into account the characteristics of this transformation matrix, as such inversion may not be appropriate if the problem is ill-posed or ill-conditioned in the sense of Hadamard [6].

While machine learning-based approaches may provide a way to intrinsically regularize this formulation, their applicability, at least in their pure form, is limited as reference data is typically unavailable. Moreover, hybrid (model- and learning-based) approaches such as algorithm unrolling [7] and deep priors [8] rely heavily on a good understanding of the system, which we aim to address here as preliminary step and solid basis for the *interpretability* of such systems.

Therefore, we propose in this work a procedure of *model-based inversion*, by exploiting the knowledge of the physics and the characteristics of interferometric systems.

In this paper, we extend the study to a wider category of interferometers, where a potentially infinite amount of interfering waves can be superimposed. For example, this is capable to also deal with a vast array of instruments based on Fabry-Pérot (FP) interferometers [9–12]; this is defined in our work as $\infty$-wave model, also known as Airy's distribution [3]. We propose to solve the inversion problem through a more powerful class of solvers, notably the Loris-Verhoeven (LV) algorithm [13] with proximal operators that better characterize the *a priori* knowledge through induced sparsity on the Fourier domain of the spectrum. While the proposed approach is iterative and hence with slower computational time with respect to the truncated singular value decomposition (TSVD) [14] and the ridge regression (RR) [15], which allow for a closed form solution, we show in the experimental section that this allows for improved performances, especially when the acquisitions are affected by noise. Our contributions can be summed up as follows: (i) we provide a preliminary analysis of the transfer matrix for spectral reconstruction based on its singular value decomposition (SVD); (ii) we interpret the choice of the inversion protocols and their regularizations.

## 2. PROPOSED METHODOLOGY

### 2.1. Problem statement

Figure 1 shows the pipeline of an interferometric acquisition towards reconstructing the spectrum. The direct model of the optical acquisition phenomenon can be characterized as: $\mathbf{y} = \mathbf{A}\mathbf{x} + \mathbf{e}$ , where: $\mathbf{x} \in \mathbb{R}^K$ (unknown) is the spectral radiance to be estimated and is ex-

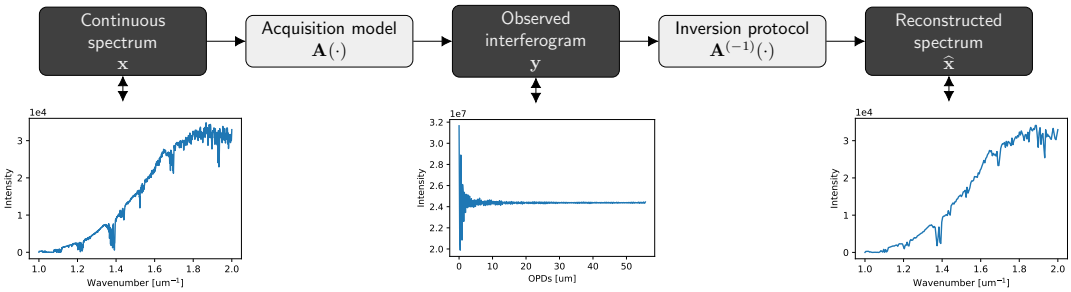


**Fig. 1**: The acquisition and inversion pipelines of the spectral reconstruction of observed interferograms from the real world

pressed in the domain of the wavenumbers $\boldsymbol{\sigma} = \{\sigma_k\}_{k\in[1,\dots,K]}$; $\mathbf{y} \in \mathbb{R}^L$ (observed) is the sampled interferogram obtained at the detector, and is expressed in the domain of the OPDs $\boldsymbol{\delta} = \{\delta_l\}_{l\in[1,\dots,L]}$; $\mathbf{A} \in \mathbb{R}^{L\times K}$ is a transfer matrix from the domain of wavenumbers to that of the OPDs; and $\mathbf{e} \in \mathbb{R}^L$ is the noise, which we assume to be Gaussian.

The goal of the inversion protocol is to estimate the value of $\mathbf{x}$. In this work, we propose to derive an estimation $\hat{\mathbf{x}}$ of the spectrum $\mathbf{x}$ by Bayesian inference [6], which is equivalent to minimize a cost function in the form:

$$\hat{\mathbf{x}} = \underset{\mathbf{x}}{\operatorname{argmin}} \frac{1}{2}\|\mathbf{y} - \mathbf{A}\mathbf{x}\|_2^2 + r(\mathbf{x}) \;, \tag{1}$$

where the right hand side is expressed as the sum of a data fidelity term and a regularization $r(\mathbf{x})$ which characterizes the *a priori* knowledge on the spectrum. In the case $r(\mathbf{x})$ is set to zero, eq.1 has a closed form solution $\mathbf{x} = \mathbf{A}^\dagger\mathbf{y}$, where $\mathbf{A}^\dagger$ denotes the pseudo-inverse of $\mathbf{A}$. We denote the rank of $\mathbf{A}$ by $R_\mathbf{A}$, which is equal to the number of non-zero singular values $\{\psi_r\}_{r\in[1,\dots,R_\mathbf{A}]}$. As the matrix $\mathbf{A}$ describes an optical transformation, some of its singular values have very small amplitudes, and consequently the singular values $\psi'_r = 1/\psi_r$ of $\mathbf{A}^\dagger$ tend to become extremely large. Hence, the condition number $c = \max(\psi_r)/\min(\psi_r)$ of $\mathbf{A}$ can either be $\infty$ or extremely large, which respectively defines either an ill-posed or an ill-conditioned problem in the sense of Hadamard.

Some simple strategies are available in the literature to avoid this problem, for which the estimation $\hat{\mathbf{x}} = \widetilde{\mathbf{A}}\mathbf{y}$ is carried out with a modified version $\widetilde{\mathbf{A}}$ of $\mathbf{A}^\dagger$, with penalized singular values. I.e.:

- In TSVD [14], only a given percentage $0 < \lambda_{\text{TSVD}} < 1$ is kept unmodified and the rest are set to zero, i.e., $\psi'_r = 1/\psi_r$ if $r < \lambda R$, and 0 otherwise.
- In RR [15], the singular values are dampened by a given penalization parameter $\lambda_{\text{RR}}$ such that $\psi'_r = \psi_r/(\psi_r^2 + \lambda_{\text{RR}}^2)$ $\forall r \in \{1,\dots,R\}$.

### 2.2. Transfer matrix discussion

Here, we provide a discussion on $\mathbf{A}$ by observing the limit of the number of reconstruction samples $K_{\max}$, after which we cannot recover new information. Providing a full analysis of the transfer matrix is out of the scope for now, so we limit the discussion to note that we choose $K_{\max} = R_\mathbf{A}$. Note that the approaches with penalization on the singular values (e.g., TSVD and RR) have an effect mainly on the small singular values (which would be responsible of noise amplification in $\mathbf{A}^\dagger$), which could already be truncated above $R_\mathbf{A}$. When this is already the case, TSVD and RR would instead affect

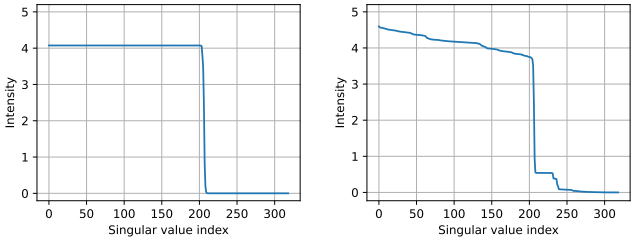


(a) 2-wave singular values (b) $\infty$-wave singular values

**Fig. 2**: Examples of the 2- and $\infty$-wave models from (2) and (3).

important information on the model, for which we propose the LV-based method in Section 2.3. Without loss of generality, we consider two transfer models based on the number of emerging waves in the interferometer [3]:

- The **2-wave model**, characterized as follows:

$$a_{lk} = (1 + \mathcal{R}^2(\sigma_k) - 2\mathcal{R}(\sigma_k)\cos(2\pi\sigma_k\delta_l))\mathcal{T}^2(\sigma_k) \tag{2}$$

- The **$\infty$-wave model**, characterized as follows:

$$a_{lk} = \frac{1}{1 + \mathcal{R}^2(\sigma_k) - 2\mathcal{R}(\sigma_k)\cos(2\pi\sigma_k\delta_l)}\mathcal{T}^2(\sigma_k) \tag{3}$$

where $\mathcal{T}$ and $\mathcal{R}$ are respectively the transmissivity and reflectivity of the surface of the interferometer.

Figure 2 shows the singular values of two examples of $\mathbf{A}$ for each wave model, sampled by $L = 319$ OPDs in the range $\delta \in [0, 0.175]$ µm, and evaluated for $\tilde{K} = 319$ wavenumbers in the range $\sigma \in [1, 2.85]$ µm$^{-1}$, with $\mathcal{R}^2(\sigma_k) = 0.13$ and $\mathcal{T}^2(\sigma_k) = 1\ \forall k$.

Looking at Figure 2a, we notice a sharp drop to 0 after index 206, so $R_\mathbf{A} \approxeq 207$. We infer that despite sampling the interferogram by 319 samples, those coming from only 207 components are linearly independent, which is the intrinsic subspace of $\mathbf{A}$. This implies that the amount of recoverable spectral information, and thus the choice of the reconstructed samples, is bounded by $K_{\max} = 207 < \tilde{K}$ samples. Looking at Figure 2b, we notice a sharp drop around index 206, then the plot progressively descends towards zero. Arguably speaking, this may be due to an aliasing effect, leading to the newly-induced low-intensity components, and increasing the intrinsic dimensionality of the sampling space. In both cases, $\mathbf{A}$ is not invertible since the zero and low-intensity singular values cause the inversion to explode.

### 2.3. Loris-Verhoeven algorithm

We propose our LV-based solution to solve the problem. The cost function of LV [13] can be expressed as follows:

$$\hat{\mathbf{x}} = \underset{\mathbf{x}}{\operatorname{argmin}}\, h(\mathbf{x}) + \lambda\, g(\mathbf{W}\mathbf{x}) \tag{4}$$

where $\lambda$ is the regularizing parameter, $h(\mathbf{x}) = \frac{1}{2}\|\mathbf{A}\mathbf{x} - \mathbf{y}\|_2^2$ is the fidelity term, $g(\cdot)$ is the regularization term, and $\mathbf{W}$ is a linear domain transformation operator.

In our case, we wish to impose a *sparse-inducing regularizer on the Fourier domain of the spectrum*, where high-frequency components (such as noise) can be softly discarded. For that, we first define $\mathbf{W} \in \mathbb{R}^{K\times K}$ as the type-II discrete cosine transform (DCT), which is an orthogonal *Fourier-related* domain such that:

$$w_{ij} = \sqrt{\frac{2}{K}} \cos\left(\frac{\pi}{K}\left(j - \frac{1}{2}\right)(i-1)\right)_{\forall i,j\in\{1,\dots,K\}} \tag{5}$$

then we choose $g(\cdot) = \|\cdot\|_1$ as the *sparsity-inducing* regularizer, which in this case becomes the $\ell_1$-norm of the DCT of $\mathbf{x}$ (i.e., minimizing the number of non-zero elements in the Fourier domain).

Now, in order to solve the problem, we choose a class of solvers based on the *proximal operators* [16] within a primal/dual problem. The goal is to minimize $h(\mathbf{x})$ while being penalized for inducing sparsity on the DCT of $\mathbf{x}$, without acting on $\mathbf{A}$ itself. That said, the primal and dual sub-problems become, respectively:

$$\hat{\mathbf{x}} = \underset{\mathbf{x}\in\mathbb{R}^K}{\operatorname{argmin}} \frac{1}{2}\|\mathbf{A}\mathbf{x} - \mathbf{y}\|_2^2 + \lambda\|\mathbf{W}\mathbf{x}\|_1 \tag{6a}$$

$$\hat{\mathbf{u}} = \underset{\mathbf{u}\in\mathbb{R}^L}{\operatorname{argmin}}\, h^\star(-\mathbf{W}^\mathsf{T}\mathbf{u}) + \lambda\, g^\star(\mathbf{u}/\lambda) \tag{6b}$$

where $\mathbf{u}$ is the so-called dual variable, and $h^\star(\cdot)$ and $g^\star(\cdot)$ are the Fenchel conjugates of $h(\cdot)$ and $g(\cdot)$ respectively [16].

For the $\ell_1$-norm, the dual norm is the $\ell_\infty$-norm, then $g^\star(\mathbf{x})$ is defined over a multi-dimensional box of size $\lambda$ defined by the $\ell_\infty$-norm [16]. Now, $\forall\, k \in \{1,\dots,K\}$, the proximal operator is:

$$\operatorname{prox}_{\lambda,g^\star}(x_k) = \begin{cases} -\lambda & \text{if } x_k < -\lambda \\ x_k & \text{if } |x_k| < \lambda \\ \lambda & \text{if } x_k > \lambda \end{cases} \tag{7a}$$

$$\iff \operatorname{prox}_{\lambda\, g^\star}(\mathbf{x}) = \min(\max(\mathbf{x}, -\lambda), \lambda) \tag{7b}$$

where $\lambda$ acts as a *thresholding operator*.

Algorithm 1 shows the LV-based updates of $\mathbf{x}$ and $\mathbf{u}$, where $\mathbf{x}^{(q)}$ denotes the update of $\hat{\mathbf{x}}$ at the $q$-th iteration. $\eta$ and $\tau$ are convergence parameters such that $\eta\tau \leq \|\mathbf{W}\| = 1$, while $1 \leq \rho \leq 2$ is the over-relaxation parameters; their specified values were chosen according to the relevant literature [17].

**Algorithm 1** Proposed method inspired by Loris-Verhoeven [13]

**Require:** $\mathbf{A}$, $\mathbf{W}$, $N_{\text{iters}}$
  **Initialize** $\mathbf{x}^{(0)} = \mathbf{A}^\mathsf{T}\mathbf{y}$, $\mathbf{u}^{(0)} = \mathbf{W}\mathbf{x}^{(0)}$
  **Initialize** $\tau = 0.99$, $\eta = 1$, and $\rho = 1.9$
  **Define** $\operatorname{prox}_{\lambda\, g^\star}(\mathbf{x}) = \min(\max(\mathbf{x}, -\lambda), \lambda)$
  **while** Stopping criterion is not met **do**
    $\mathbf{e}_x^{(q)} = \mathbf{A}^\mathsf{T}(\mathbf{A}\mathbf{x}^{(q)} - \mathbf{y})$
    $\mathbf{x}^{(q+\frac{1}{2})} = \mathbf{x}^{(q)} - \tau\left(\mathbf{e}_x^{(q)} + \mathbf{W}^\mathsf{T}\mathbf{u}^{(q)}\right)$
    $\mathbf{u}^{(q+\frac{1}{2})} = \operatorname{prox}_{\lambda,g^\star}\left(\mathbf{u}^{(q)} + \eta\mathbf{W}\mathbf{x}^{(q+\frac{1}{2})}\right)$
    $\mathbf{x}^{(q+1)} = \mathbf{x}^{(q)} - \rho\tau\left(\mathbf{e}_x^{(q)} + \mathbf{W}^\mathsf{T}\mathbf{u}^{(q+\frac{1}{2})}\right)$
    $\mathbf{u}^{(q+1)} = \mathbf{u}^{(q)} + \rho\left(\mathbf{u}^{(q+\frac{1}{2})} - \mathbf{u}^{(q)}\right)$
  **end while**
  **return** $\hat{\mathbf{x}} = \mathbf{x}^{(N_{\text{iters}})}$

## 3. EXPERIMENTS AND RESULTS

### 3.1. Experimental setup

For the experiments, we acquire three real spectral datasets of two main targets, described in Table 1 in details. The two targets are:

- The **Sun**: 1 dataset of 22 solar spectra acquired at different times of the day.
- X-rite's ColorChecker (CC): 2 datasets of the CC's 24 squares spectra by two spectrometers, **SHINE** and **SPECIM**.

| Dataset | No. of spectra, $N$ | No. of samples, $K$ | Wavenumber range, $\sigma$ ($\mu$m$^{-1}$) | $R_{\mathbf{A}}$, $K_{\max}$ |
|---|---|---|---|---|
| **Sun** | 22 | 319 | $[1, 2]$ | 113 |
| **SHINE** | 24 | 276 | $[0.67, 2.5]$ | 206 |
| **SPECIM** | 24 | 204 | $[1, 2.5]$ | 169 |

**Table 1**: Information on the available spectral datasets. $R_{\mathbf{A}}$ is calculated given a transfer matrix of an instrument with $L = 319$ OPDs in the range $\delta \in [0, 0.175]$ µm, and given the respective $K$ and $\sigma$.

In the experiments, the physical and optical parameters of $\mathbf{A}$ follow the characterization of a real interferometric snapshot imaging spectrometer: the Imaging SPectrometer On Chip (ImSPOC) UV2 model, which is composed of 319 FP interferometers, corresponding to $L = 319$ OPDs in the range $\delta \in [0, 0.175]$ µm. We separate between two types of the transfer model:

- $\mathbf{A}_{\text{sim}}$: Used in the *forward* process for the *simulation* of the observations $\mathbf{Y} \in \mathbb{R}^{L\times N}$ from the real spectral datasets $\mathbf{X} \in \mathbb{R}^{K\times N}$ such that $\mathbf{Y} = \mathbf{A}_{\text{sim}}\mathbf{X}$. The real spectra are kept raw so that the process is as close to reality as possible.
- $\mathbf{A}$: Used in the *backward* process for the *inversion* of the observations into the estimated spectra $\hat{\mathbf{X}} \in \mathbb{R}^{K\times N}$. As discussed in Section 2.2, we choose $K = R_{\mathbf{A}}$.

Moreover, we consider high and low levels of Gaussian noise corresponding to SNR values of $\{60, 50, 40\}$ dB to better assess the inversion protocols. The comparison with the reference is done using the Root Mean Squared Error (RMSE).

### 3.2. Results and discussion

Table 2 shows the results of the three inversion protocols, applied on the three datasets, under the 2- and $\infty$-wave models and the aforementioned SNR values. For each case, we perform the tests with many values of the regularizing parameters within reasonable ranges. Specifically, we run each case with 225 values of $\lambda_{\text{TSVD}} \in [0.2, 1]$, 225 values of $\lambda_{\text{RR}} \in [0, 20]$, and 225 values of $\lambda_{\text{LV}} \in \log_{10}([-3, -0.0001])$, then we report the minimum RMSE and the corresponding regularizing parameter $\lambda_{\min}$ in the table.

#### *3.2.1. Rank deficiency*

Following the discussion on the number of reconstruction samples and the rank of $\mathbf{A}$ in Section 2.2, Figure 3 shows the progress of RMSE for each method as the regularization parameter traverses its

| | | 2-**wave model** (e.g. Michelson-based) | | | | | | $\infty$-**wave model** (e.g. FP-based) | | | | | |
|---|---|---|---|---|---|---|---|---|---|---|---|---|---|
| | | **SNR** $= 60$ dB | | **SNR** $= 50$ dB | | **SNR** $= 40$ dB | | **SNR** $= 60$ dB | | **SNR** $= 50$ dB | | **SNR** $= 40$ dB | |
| **Dataset** | **Method** | $\lambda_{\min}$ | RMSE | $\lambda_{\min}$ | RMSE | $\lambda_{\min}$ | RMSE | $\lambda_{\min}$ | RMSE | $\lambda_{\min}$ | RMSE | $\lambda_{\min}$ | RMSE |
| **Sun** | TSVD [14] | 0.9786 | 0.0782 | 0.9786 | 0.1140 | 0.9786 | 0.2632 | 0.9964 | 0.0881 | 0.9964 | 0.1212 | 0.9000 | 0.2649 |
| | RR [15] | 10.8036 | 0.0784 | 13.6607 | 0.1143 | 20.0000 | 0.2644 | 2.5001 | 0.0864 | 3.3929 | 0.1188 | 20.0000 | 0.2612 |
| | Proposed | 0.0534 | **0.0680** | 0.0643 | **0.0800** | 0.2655 | **0.1124** | 0.0358 | **0.0716** | 0.0727 | **0.0823** | 0.2824 | **0.1116** |
| **SHINE** | TSVD [14] | 0.9929 | 0.0584 | 0.9893 | 0.1505 | 0.9357 | 0.3229 | 0.9929 | 0.0721 | 0.9929 | 0.1536 | 0.9929 | 0.3176 |
| | RR [15] | 11.1608 | 0.0582 | 14.5536 | 0.1508 | 19.1071 | 0.3266 | 2.5894 | 0.0705 | 1.5179 | 0.1543 | 0.0001 | 0.3177 |
| | Proposed | 0.0240 | **0.0474** | 0.1478 | **0.0842** | 0.6104 | **0.1493** | 0.0347 | **0.0639** | 0.1672 | **0.0860** | 0.3294 | **0.1444** |
| **SPECIM** | TSVD [14] | 0.9929 | 0.0507 | 0.9929 | 0.1203 | 0.9036 | 0.2115 | 0.9929 | **0.0566** | 0.9929 | 0.1211 | 0.9929 | 0.2191 |
| | RR [15] | 4.2858 | 0.0506 | 9.0179 | 0.1203 | 19.0179 | 0.2120 | 2.6787 | 0.0604 | 1.3394 | 0.1235 | 0.0001 | 0.2202 |
| | Proposed | 0.0165 | **0.0459** | 0.1433 | **0.0807** | 0.3003 | **0.1394** | 0.0255 | 0.0604 | 0.1524 | **0.0823** | 0.2824 | **0.1427** |

**Table 2**: The results obtained from the three inversion protocols applied on the three datasets under the 2- and $\infty$-wave models and different SNR values. For each case, we report the minimum RMSE and its regularizing parameter $\lambda$. The best RMSE values are marked in **bold**.

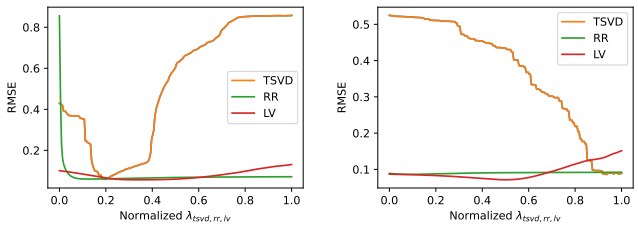


(a) $K = L = 319$ (b) $K = K_{\max} = 113$

**Fig. 3**: RMSE plots with respect to the regularization parameter of each method for different numbers of reconstruction samples $K$. Since the ranges of $\lambda$ are different for each method (see Section 3.2), for the sake of visibility, they are normalized into the range $[0, 1]$ such that $\lambda_{\text{plot}} = (\lambda - \lambda_{\min})/(\lambda_{\max} - \lambda_{\min})$.

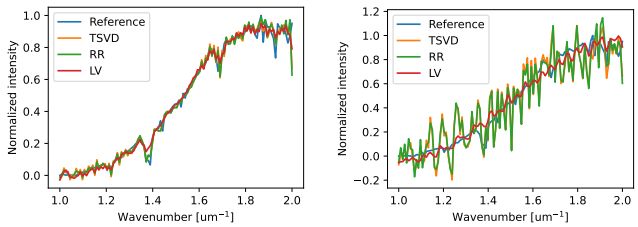


(a) SNR $= 60$ dB (b) SNR $= 40$ dB

**Fig. 4**: Reconstruction of a solar spectrum under the $\infty$-wave model for different SNR levels.

respective range for the reconstruction of a solar spectrum, under the $\infty$-wave model, at 60 dB SNR.

In Figure 3a, we notice that TSVD shows a minimum RMSE at $\lambda_{\text{TSVD}} = 0.357$, which considers only $\lambda_{\text{TSVD}} * 319 \approxeq 113$ singular values, which is exactly at $K_{\max}$. In Figure 3b, as we already choose $K = K_{\max}$, TSVD shows a minimum RMSE at $\lambda_{\text{TSVD}}$ that is the closest to 1, which also clearly shows in Table 2 *for all* the TSVD cases. The main reason behind this observation is that there are very few to no singular values that would tend to zero. Moreover, in the case of RR, the RMSEs are very close to each others over the tested range of $\lambda_{\text{RR}}$, so there is barely any pattern to be observed, which also reflects in Table 2 *for all* the RR cases.

In both figures, our proposed LV-based method shows the best overall RMSE progress and the lowest minimum values. This further supports the reliance on methods that reduce the noise without directly affecting important information in the model.

### *3.2.2. Comparison with conventional methods: RMSE, and robustness to noise*

In Table 2, at a first glance, we notice that LV has the best overall performance (i.e., minimum RMSEs), while those of TSVD and RR are very close to each others. For SNR $= 60$ dB, the performance of LV is only slightly better than those of TSVD and RR, but the difference becomes quite significant as we move towards SNR $= 40$ dB with around half the RMSE on average or even less.

As the noise increases, unlike TSVD and RR, we notice that the values of $\lambda_{min}$ *for all* the LV cases increase, marking an increasing reliance on the regularization component, which induces sparsity on the DCT domain of the spectrum and attempts to threshold the noise components. However, this also means that applying higher penalization for the favor of the induced sparsity further smooths out the spectrum, which is a trade-off that has to be taken into account. This clearly shows in Figure 4, which shows a comparison between the reconstructed spectra of a solar spectrum under different SNR levels, showing a significant advantage in the favor of the proposed method.

## 4. CONCLUSION

In this work, we proposed a model-based solution for the spectral reconstruction of interferometric acquisitions of the $\infty$-wave model based on a powerful class of solvers, including a preliminary discussion on the properties of the transfer matrix, as well as the choice of the LV algorithm with proximal operators for inducing sparsity on the Fourier domain of the desired spectrum. This work still shows several challenges, notably the occurring mismatches at increasing noise levels, where the high penalization of LV tends to further smooth the spectrum, and the scarcity of real reference data for learning-based approaches.

That said, this work proposes several future directions. First, we plan to provide more real data from real instruments, most of which are prototypes at the moment. Second, we plan to test this same framework on real interferograms. Third, one could investigate the use of collaborative Total Variation [18] for the inversion of full images. Finally, this work is meant to also be a stepping stone towards learning-based approaches to better characterize real-world parameters that might be missing from the model-based knowledge.

## 5. REFERENCES


[1] Michael T. Eismann, *Hyperspectral remote sensing*, Press Monographs. Society of Photo-Optical Instrumentation Engineers, 2012.

[2] Dimitris Manolakis, Ronald Lockwood, and Thomas Cooley, *Hyperspectral imaging remote sensing: physics, sensors, and algorithms*, Cambridge University Press, 2016.

[3] Eugene Hecht, *Optics (5th edition)*, Pearson, 2016.

[4] Parameswaran Hariharan, *Basics of interferometry*, Elsevier, 2010.

[5] Marco Donatelli and Stefano Serra-Capizzano, Eds., *Computational methods for inverse problems in imaging*, Springer-Verlag GmbH, 2019.

[6] Jérôme Idier, *Bayesian approach to inverse problems*, John Wiley & Sons, 2013.

[7] Vishal Monga, Yuelong Li, and Yonina C Eldar, "Algorithm unrolling: Interpretable, efficient deep learning for signal and image processing," *IEEE Signal Processing Magazine*, vol. 38, no. 2, pp. 18–44, 2021.

[8] Kai Zhang, Yawei Li, Wangmeng Zuo, Lei Zhang, Luc Van Gool, and Radu Timofte, "Plug-and-play image restoration with deep denoiser prior," *IEEE Transactions on Pattern Analysis and Machine Intelligence*, 2021.

[9] S Gousset, D Picone, E Le Coarer, JM Rodrigo, D Voisin, L Croize, Y Ferrec, and M Dalla Mura, "Imspoc: A novel compact hyperspectral camera for the monitoring of atmospheric gases," in *IGARSS 2022-2022 IEEE International Geoscience and Remote Sensing Symposium*. IEEE, 2022, pp. 5293–5296.

[10] Massimo Zucco, Marco Pisani, Valentina Caricato, and Andrea Egidi, "A hyperspectral imager based on a fabry-perot interferometer with dielectric mirrors," *Optics express*, vol. 22, no. 2, pp. 1824–1834, 2014.

[11] Yaniv Oiknine, Isaac August, and Adrian Stern, "Multi-aperture snapshot compressive hyperspectral camera," *Opt. Lett.*, vol. 43, no. 20, pp. 5042–5045, Oct 2018.

[12] Marco Pisani and Massimo Zucco, "Compact imaging spectrometer combining fourier transform spectroscopy with a fabry-perot interferometer," *Optics express*, vol. 17, no. 10, pp. 8319–8331, 2009.

[13] Ignace Loris and Caroline Verhoeven, "On a generalization of the iterative soft-thresholding algorithm for the case of non-separable penalty," *Inverse Problems*, vol. 27, no. 12, pp. 125007, 2011.

[14] Per Christian Hansen, "Truncated singular value decomposition solutions to discrete ill-posed problems with ill-determined numerical rank," *SIAM Journal on Scientific and Statistical Computing*, vol. 11, no. 3, pp. 503–518, 1990.

[15] Gene H Golub, Per Christian Hansen, and Dianne P O'Leary, "Tikhonov regularization and total least squares," *SIAM journal on matrix analysis and applications*, vol. 21, no. 1, pp. 185–194, 1999.

[16] Neal Parikh, Stephen Boyd, et al., "Proximal algorithms," *Foundations and trends® in Optimization*, vol. 1, no. 3, pp. 127–239, 2014.

[17] Laurent Condat, Daichi Kitahara, Andrés Contreras, and Akira Hirabayashi, "Proximal splitting algorithms for convex optimization: A tour of recent advances, with new twists," *arXiv e-prints*, pp. arXiv–1912, 2019.

[18] Joan Duran, Michael Moeller, Catalina Sbert, and Daniel Cremers, "Collaborative total variation: a general framework for vectorial tv models," *SIAM Journal on Imaging Sciences*, vol. 9, no. 1, pp. 116–151, 2016.